NASA Technical Memorandum 79036

FRACTURE MODES IN OFF-AXIS FIBER COMPOSITES

J. H. Sinclair and C. C. Chamis
Lewis Research Center
Cleveland, Ohio 44135

TECHNICAL PAPER to be presented at the
Thirty-fourth Annual Conference of the SPI
Reinforced Plastics/ Composites Institute
New Orleans, Louisiana, January 29 - February 2, 1979

CONTENTS

FRACTURE MODES IN OFF-AXIS FIBER COMPOSITES

by J. H. Sinclair* and C. C. Chamis*

National Aeronautics and Space Administration
Lewis Research Center
Cleveland, Ohio 44135

E-9836

SUMMARY

Criteria have been developed for identifying, characterizing, and quantifying fracture modes in high-modulus graphite-fiber/resin unidirectional composites subjected to off-axis tensile loading. Procedures are described which use sensitivity analyses and off-axis data to determine the uniaxial strength of fiber composites. It was found that off-axis composites fail by three fracture modes which produce unique fracture surface characteristics. The stress that dominates each fracture mode and the load angle range of its dominance can be identified. Linear composite mechanics is adequate to describe quantitatively the mechanical behavior of off-axis composites. The uniaxial strengths predicted from off-axis data are comparable to those measured in uniaxial tests.

INTRODUCTION

A detailed investigation was conducted at NASA-LeRC of the mechanical behavior of high-modulus graphite-fiber/epoxy-matrix unidirectional composites subjected to off-axis tensile loading (refs. 1 and 2). The objectives of this investigation were to: (1) identify and characterize fracture surfaces, (2) determine whether linear composite mechanics can be used with confidence to describe quantitatively the mechanical behavior of off-axis composites subjected to tensile loading, (3) identify and quantify fracture modes associated with off-axis fractures, (4) develop criteria and convenient procedures which can be used to identify and quantify fracture modes associated with off-axis loading, (5) use sensitivity analyses in conjunction with off-axis fracture data to determine uniaxial strength indirectly, and (6) assess the effects that possible eccentricities

*Aerospace Engineer, Composites and Structures Branch, NASA Lewis Research Center, Cleveland, Ohio 44135.

(that could arise during testing) may have on the fracture stress of off-axis specimens. The investigation consisted of mechanical testing, scanning electron microscopy (fractographic) studies, composite mechanics, and finite element analyses including NASTRAN.

The fractographic studies (item (1) above) were reported in detail in reference 3. The effects of possible eccentricities (item (6) above) were reported in detail in reference 4. The part of the investigation of the application of composite mechanics, identification and quantification of fracture modes, criteria and convenient procedures for identifying fracture modes, sensitivity studies (items (2) to (5) above) and the results obtained are described in detail herein. The description is divided into an experimental section and a theoretical and comparisons section. The latter section is subdivided into sections on elastic constants, fracture stresses and strains, ply fracture stresses and strains, regions of single-failure mode predominance, stress-type influence on fracture mode, and sensitivity studies.

EXPERIMENTS

The laminate used in this investigation consisted of eight unidirectional plies of Modmor-I graphite fibers about 50 percent by volume in a matrix of ERLA-4617 epoxy resin cured with metaphenylene di-amine (MPDA). Tensile specimens were cut from the laminate plate at the desired load angles as shown in figure 1 by use of a diamond cutting wheel. Stacks of specimens, so cut, were placed on edge and dressed down to the required 1.27 centimeter (0.500-in.) width by a diamond grinding wheel. Specimen ends were reinforced with adhesively-bonded, tapered fiber glass tabs. The tensile specimens were then instrumented with either two or five 120-ohm, 60° delta-rosette strain gages. A schematic of specimen geometry and strain gage arrangement is shown in figure 2. The test specimens were loaded to fracture by using a hydraulically actuated universal testing machine. Loading was incremental to facilitate periodic recording of strain gage data. Fractured surfaces of the tensile specimens were observed by scanning electron microscopy, and typical phoromicrographs were made to illustrate fracture modes as will be described later.

A photograph of the fractured specimens is presented in figure 3. The load angles, between load and fiber directions of the specimens from bottom to top in the figure are: 0°, 5°, 10°, 15°, 30°, 45°, 60°, 75°, and 90°. Note that the specimens tested at 0°, 5°, 10°, 15°, and 30° off-axis fractured away from

the end tabs and those tested at 45°, 60°, 75°, and 90° fractured near the end tab. Fractures at or near end tabs are to be expected. Finite-element analysis results (refs. 2 and 4) show that the stresses at the edge near the end tab are higher than at the mid-length center in certain orientations. Consequently, these stresses can initiate fractures near the end-tab region.

Tensile properties determined during this study are summarized in Table I. The specimens tested along the fiber direction broke at 56.3×10^3 N/cm^2 (81.7 ksi) and the fracture strengths of the specimens decreased gradually with increasing load angle; the transverse specimen (90° off-axis) broke at 2.8×10^3 N/cm^2 (4 ksi). The moduli also decreased with increasing load angle and lie between about 24×10^6 N/cm^2 (35×10^6 psi) for the longitudinal specimen (0° off-axis) and just over 0.75×10^6 N/cm^2 (1.1×10^6 psi) for the 90° off-axis specimen. Stress strain curves (from gage 2, fig. 2) are presented in figure 4. Note that they are all linear to fracture.

The fractured surfaces of the specimens were studied by using scanning electron microscopy (SEM). The photomicrographs of the fracture surfaces exhibit unique characteristics in different load angle (θ) ranges. The details are presented in references 1 and 3. Photomicrographs from these references relevant to this discussion will be described later.

THEORY AND COMPARISONS WITH EXPERIMENTS

Linear composite mechanics (LCM) was used to predict the elastic constants, composite fracture stresses and strains, ply fracture stresses and strains, and region boundaries of single-failure-mode predominance. Linear composite mechanics is applicable and sufficient since the stress strain curves to fracture are linear (fig. 4). Comparisons are made between predicted results and measured data to show that LCM describes quantitatively the mechanical behavior of the various specimens. And, thus LCM can be used with confidence to quantify the different fracture modes and their range of predominance.

Elastic Constants

The elastic constants of interest in this investigation are the modulus of elasticity along the load direction E_{cxx}, the Poisson's ratio ν_{cxy}, and the

shear coupling coefficient ν_{cxs}, which is a measure of the shear deformation induced by the stress along the load, or x direction. These elastic constants, E_{cxx}, ν_{cxy}, and ν_{cxs}, are expressed in terms of unidirectional composite elastic constants by using well known transformation equations. The equations used are

$$\frac{1}{E_{cxx}} = \frac{\cos^4\theta}{E_{\ell 11}} + \frac{\sin^4\theta}{E_{\ell 22}} + \frac{1}{4}\left(\frac{1}{2G_{\ell 12}} - \frac{\nu_{\ell 12}}{E_{\ell 11}}\right)\sin^2 2\theta \tag{1}$$

$$\frac{\nu_{cxy}}{E_{cxx}} = -\frac{1}{4}\left(\frac{1 + 2\nu_{\ell 12}}{E_{\ell 11}} + \frac{1}{E_{\ell 22}} - \frac{1}{G_{\ell 12}}\right)\sin^2 2\theta + \frac{\nu_{\ell 12}}{E_{\ell 11}} \tag{2}$$

$$\frac{\nu_{cxs}}{E_{cxx}} = \left(\frac{1 + \nu_{\ell 12}}{E_{\ell 22}}\sin^2\theta - \frac{1 + \nu_{\ell 12}}{E_{\ell 11}}\cos^2\theta + \frac{\cos 2\theta}{2G_{\ell 12}}\right)\sin 2\theta \tag{3}$$

where θ is the angle between fiber and load directions, $E_{\ell 11}$ denotes the modulus of elasticity along the fiber directions, $E_{\ell 22}$ is the modulus of elasticity transverse to the fiber direction, $G_{\ell 12}$ is the in-plane (intralaminar) shear modulus, and $\nu_{\ell 12}$ is the major Poisson's ratio. The subscript ℓ identifies the unidirectional property and the subscripts 1 and 2 denote orthogonal material axes with 1 taken along the fiber direction. Equations (1), (2), and (3) are programmed in the computer code (ref. 5) that was used to predict the elastic constants from the unidirectional composite properties. The predicted properties were than used for comparison with the measured data.

The comparison for the modulus E_{cxx} is shown in figure 5 and shows very good agreement. The comparison for the Poisson's ratio is shown in figure 6. As can be seen, the measured data are below the predicted curve in the load-angle range $0^\circ < \theta < 45^\circ$. The agreement is good at load angles greater than 45°. The comparison for the coupling coefficient ν_{cxs} is shown in figure 7. Again, the agreement is very good except possibly for θ angles less than 15°.

Fracture Stresses and Strains

The composite fracture stress S_{cxx} along the load direction for the specimens was predicted by using the following equations:

$$S_{cxx} \frac{1}{\left[\frac{\cos^4\theta}{S_{\ell 11T}^2} + \frac{\sin^4\theta}{S_{\ell 22T}^2} + \frac{1}{4}\left(\frac{1}{S_{\ell 12S}^2} - \frac{K_{\ell 12}}{S_{\ell 11T}S_{\ell 22T}}\right)\sin^2 2\theta\right]^{1/2}} \tag{4}$$

$$K_{\ell 12} = K'_{\ell 12} \frac{(1 + 4\nu_{\ell 12} - \nu_{\ell 13})E_{\ell 22} + (1 - \nu_{\ell 23})E_{\ell 11}}{\left[E_{\ell 11}E_{\ell 22}(2 + \nu_{\ell 12} + \nu_{\ell 13})(2 + \nu_{\ell 21} + \nu_{\ell 23})\right]^{1/2}} \tag{5}$$

The undefined notation in equations (4) and (5) is as follows: $K'_{\ell 12}$ is a correlation coefficient (ref. 6) which is assumed to be unity in this case, $S_{\ell 11T}$ is the uniaxial longitudinal fracture stress (along the fiber), $S_{\ell 22T}$ is the uniaxial transverse fracture stress, $S_{\ell 12S}$ is the uniaxial intralaminar (in-plane) shear fracture stress, and $\nu_{\ell 13}$ and $\nu_{\ell 23}$ represent Poisson's ratio in direction 3, which is through the composite thickness. The Poisson's ratio $\nu_{\ell 13}$ is usually taken equal to $\nu_{\ell 12}$, and $\nu_{\ell 23}$ is computed using composite micromechanics. The value of $K_{\ell 12}$ for the high-modulus, graphite-fiber/epoxy (Mod I/E) composite, computed by the computer code (ref. 5), is 1.44. Note that equations (4) and (5) are derivable from a modified distortion energy principle described in reference 6.

The composite fracture strains ε_c along the load direction for the specimens were predicted by using the following equations:

$$\varepsilon_{cxx} = \frac{S_{cxx}}{E_{cxx}} \tag{6}$$

$$\varepsilon_{cyy} = \nu_{cxy}\frac{S_{cxx}}{E_{cxx}} \tag{7}$$

$$\varepsilon_{cxy} = \nu_{cxs}\frac{S_{cxx}}{E_{cxx}} \tag{8}$$

where S_{cxx} is given by P/A (where P is the fracture load and A the specimen cross section area) and the elastic constants are determined by using equations (1) to (3). Equations (4) to (8) have also been programmed in the computer code (ref. 5), and the predicted results used for the comparisons were generated by using this code.

The comparison of predicted and measured values of fracture stress is shown in figure 8. The unidirectional composite fracture stresses used to generate the predicted data are also shown in this figure. As can be seen the comparison is excellent. The comparisons for the center gage fracture strains are summarized in table II. The comparison is reasonably good for the axial ε_{cxx} and shear ε_{cxy} strains, and it is relatively poor for the Poisson's ε_{cyy} strain, perhaps because of the relatively small numerical values of the Poisson's ratio for composites in general. The good agreement for ε_{cxx} and ε_{cxy} was anticipated since the stress-strain curves are linear (or nearly so) to fracture, as was already mentioned.

The important conclusion from these comparisons is that the off-axis failure of composites with linear stress-strain curves to fracture is predicted accurately by the failure theory summarized herein and described in detail in reference 6.

Ply Fracture Stresses and Strains

The ply fracture stresses were determined by using the following equations:

$$\sigma_{\ell 11} = S_{cxx} \cos^2\theta \tag{9}$$

$$\sigma_{\ell 22} = S_{cxx} \sin^2\theta \tag{10}$$

$$\sigma_{\ell 12} = \frac{1}{2} S_{cxx} \sin 2\theta \tag{11}$$

where σ_ℓ represents ply stress and the numerical subscripts the directions.

The ply fracture strains ε_ℓ were determined using the following matrix equation:

$$\begin{Bmatrix} \varepsilon_{\ell 11} \\ \varepsilon_{\ell 22} \\ \varepsilon_{\ell 12} \end{Bmatrix} = \begin{bmatrix} \cos^2\theta & \sin^2\theta & \frac{1}{2}\sin 2\theta \\ \sin^2\theta & \cos^2\theta & -\frac{1}{2}\sin 2\theta \\ -\sin 2\theta & \sin 2\theta & \cos 2\theta \end{bmatrix} \begin{Bmatrix} \varepsilon_{cxx} \\ \varepsilon_{cyy} \\ \varepsilon_{cxy} \end{Bmatrix} \tag{12}$$

where ε_c are the composite strains at fracture which are determined from equations (6) to (8). Equations (9) to (12) are also available in the computer code (ref. 5). The predicted results reported herein were generated by using this code.

Regions of Single-Failure Mode Predominance

The regions where single failure modes predominate may be identified by plotting the following ratios from measured data: $\sigma_{\ell 11}/S_{\ell 11T}$, $\sigma_{\ell 22}/S_{\ell 22T}$, $\sigma_{\ell 12}/S_{\ell 12S}$, $\epsilon_{\ell 11}/\varepsilon_{\ell 11T}$, $\epsilon_{\ell 22}/\varepsilon_{\ell 22T}$, and $\epsilon_{\ell 12}/\varepsilon_{\ell 12S}$ as functions of load and angle θ. In these ratios σ_ℓ and ϵ_ℓ denote ply stress and strain, respectively, and S_ℓ and ε_ℓ represent the corresponding uniaxial fracture stress and strain, respectively. Regions of single-failure-mode predominance show that both of these ratios (σ_ℓ/S_ℓ) and ($\epsilon_\ell/\varepsilon_\ell$) associated with this failure mode are near unity. Those ratios associated with the other two failure modes are considerably smaller by comparison.

The resulting plot for stress is shown in figure 9. As can be observed from this figure, the curve for $\sigma_{\ell 11}/S_{\ell 11}$ is closer to unity than $\sigma_{\ell 22}/S_{\ell 22}$ or $\sigma_{\ell 12}/S_{\ell 12}$, in the load-angle range $0^\circ \leq \theta < 5^\circ$; therefore, longitudinal tension is the predominant fracture mode in this range. The scanning electron microscope (SEM) photomicrographs show that the fracture surface in this region is a tiered surface, dominated by fiber fractures (fig. 10(a)) (from ref. 3). The ratio $\sigma_{\ell 12}/S_{\ell 12}$ is closer to unity as observed from the crossover points in the range $5^\circ < \theta \leq 20^\circ$, indicating that intralaminar shear stress is the predominant fracture mode in this range. The SEM photomicrographs show that the fracture surface in this region is dominated by matrix lacerations (fig. 10(b)). The ratio $\sigma_{\ell 22}/S_{\ell 22}$ is closer to unity as observed

from the crossover points in the range $45^0 \leq \theta \leq 90^0$ indicating that the transverse tensile stress is the predominant fracture mode in this range. The SEM photomicrographs show that the fracture surface is dominated by matrix cleavage and fiber surfaces free from matrix residue (fig. 10(c)). The ratios σ_{f12}/S_{f12S} and σ_{f22}/S_{f22T} have comparable magnitudes in the load angle range $20^0 < \theta < 45^0$. In this range, then, fracture is produced by combinations of intralaminar shear and transverse tensile stresses (mixed mode). The SEM photomicrographs show that the fracture surface in this range is a mixture of matrix lacerations, matrix cleavage, and fiber surface free of matrix residue (fig. 10(d)).

The corresponding plot for strains is shown in figure 11. As can be observed in this figure the ratios for strains near unity are the same as those for the corresponding stresses. The load angle in which the individual strains dominate are longitudinal tension $0^0 \leq \theta < 5^0$, intralaminar shear $5^0 < \theta \leq 20^0$, transverse tension $45^0 \leq \theta \leq 90^0$, and mixed mode (combinations of intralaminar shear and transverse tensile $(20^0 < \theta < 45^0$.

The dominance of longitudinal tensile fracture stress for the narrow load angle range below 5^0 is well known in the fiber composite community. However, the narrow range (about 15^0) of intralaminar shear stress fracture dominance and the large range (about 60^0) of transverse tensile stress fracture stress dominance have not been identified or, at least, not reported prior to the investigation described in references 1 and 2. It is important to note at this juncture that the results of figures 9 and 11 provided the theoretical basis for using the 10^0 off-axis tensile test method for intralaminar shear characterization (ref. 7). This test method was a spinoff of the same investigation.

The major conclusion from this discussion is that the regions of single-stress-fracture-mode dominance can be identified by normalized plots of stress and strain. And, furthermore, in these regions the fracture surface SEM photomicrographs show distinct fracture mode characteristics, that is, fiber tensile fracture $0^0 \leq \theta < 5^0$, matrix lacerations $5^0 < \theta \leq 20^0$, mixed modes $20^0 < \theta < 45^0$, and matrix cleavage $45^0 \leq \theta \leq 90^0$.

Stress-Type Influence on Fracture Mode

A procedure to identify regions of individual stress influence on fracture mode is obtained by normalizing the ply stresses with respect to frac-

ture stress in the load direction using equations (9) to (11). As can be seen from these equations the normalization leads to the following trigonometric functions: $\cos^2\theta$ for longitudinal stress, $\sin^2\theta$ for transverse stress, and $(\sin 2\theta)/2$ for intralaminar shear stress. The next step is to plot these functions versus load angle and superimpose the corresponding measured data. The ranges of single-stress-fracture-mode predominance are then identified by the coincidence of the measured data with the corresponding trigonometric function.

This procedure is illustrated graphically in figure 12. The following are observed in figure 12:

(1) The intralaminar shear stress coincides with its corresponding trigonometric function in the load-angle range $0^\circ < \theta \leq 20^\circ$ and, therefore, has significant influence in this range.

(2) The transverse stress coincides with its corresponding trigonometric function throughout the range of the load angle. It, therefore, influences the fracture mode throughout the range and predominates in the $30^\circ < \theta \leq 90^\circ$ range.

(3) The longitudinal stress coincides with its corresponding trigonometric function only at the 0° load angle. It, therefore, has insignificant influence in the fracture mode in the $0^\circ < \theta \leq 90^\circ$ range.

The conclusion here is that the ranges of individual stress influence and/or predominance on fracture mode are identified by means of the procedure illustrated in figure 12. The results just described coupled with the results of the scanning electron microscopy studies should be helpful for identifying, characterizing, and quantifying fracture modes in off-axis composites. Further, the results should aid in establishing comparable procedures for angle-plied laminates.

Sensitivity Studies

Uniaxial fracture stresses may be approximated indirectly by use of off-axis tensile data in conjunction with equation (4). This provides values for these stresses that are independent of uniaxial tests. To evaluate the uniaxial fracture stresses indirectly, known values for two of the three uniaxial fracture stresses ($S_{\ell 11T}$, $S_{\ell 22T}$, or $S_{\ell 12S}$) are substituted into equation (4). The equation is then used to generate curves for the composite fracture stress, S_{cxx}, with assumed values of the third uniaxial fracture stress and different

load angles θ. An approximation to the actual value of the assumed stress is then obtained by superimposing on these curves the measured values for S_{cxx}.

The procedure is illustrated graphically in figure 13, for the intralaminar shear fracture stress. The intralaminar shear stress is determined by drawing a best-fit (by eye) vertical line of the measured data (dashed line). The intralaminar shear fracture stress, or strength, is the intersection of this vertical line with the abscissa. For the Mod I E this value is 5.5×10^3 newtons per square centimeter (N/cm^2; 8 ksi), which is very close to that of the 10° off-axis tensile specimen and is within the range of available data in the literature (5.2×10^3 to 6.2×10^3 N/cm^2 (7.5 to 9.0 ksi, ref. 3)).

The same procedure can be used to determine indirectly the other uniaxial strengths. Though details are not presented here, application of this procedure yielded 2.9×10^3 N/cm^2 (4.2 ksi) for the transverse tensile strength ($S_{\ell 22T}$) of Mod I E compared to 2.75×10^3 N/cm^2 (4.0 ksi) from the 90° tensile specimen test and as high as 70×10^3 N/cm^2 (102 ksi) for the longitudinal tensile strength ($S_{\ell 11T}$), compared to 56.5×10^3 N/cm^2 (82 ksi) from the 0° tensile specimen test. One interpretation from these results is that the longitudinal tensile strength as measured from the 0° tensile specimen may be conservative. The procedure was also applied to the data for boron-epoxy reported in reference 8. The value obtained for the intralaminar shear strength was about 7.0×10^3 N/cm^2 (10.2 ksi) compared to 7.7×10^3 N/cm^2 (11.2 ksi) from the 10° off-axis.

The graphical results from sensitivity studies provide additional information. For example, from figure 13, it is seen that: (1) the curves show that an intralaminar shear strength ($S_{\ell 12S}$) greater than 6.9×10^3 N/cm^2 (10 ksi) has negligible influence on off-axis strength (S_{cxx}) for load angles θ equal to 5°, 30°, and 45°; (2) the dependence of S_{cxx} on $S_{\ell 12S}$ is significant and is almost linear for θ equal to 10° and 15° and, therefore, these test specimens are suitable for determining the intralaminar shear characteristics of unidirectional composites; and (3) the intercept of the best fit vertical line with the 5° curve yields an off-axis strength of about 45×10^3 N/cm^2 (65 ksi) for S_{cxx} which indicates that the 5° off-axis tensile specimen may have failed prematurely. The reader can probably observe additional significant information in figure 13.

SUMMARY OF RESULTS AND CONCLUSIONS

The major results of an investigation into the mechanical behavior and the fracture modes of high modulus graphite-fiber/epoxy matrix (Modmor I/epoxy fiber) composites subjected to off-axis tensile loadings are

1. The stress-strain curves to fracture are linear

2. The results predicted by linear composite mechanics were in very good agreement with measured data.

3. Composite fracture stresses predicted by using a modified distortion energy criterion were in excellent agreement with measured data.

4. A convenient plotting procedure was developed that can be used to identify which stress dominates off-axis tensile fracture.

5. The fracture modes that predominate for various ranges of load-angle were identified as follows:

   a. Longitudinal tensile (fiber breaks) near 0° load angle
   b. Intralaminar shear (matrix shear fracture) in the 5° to 20° load-angle range.
   c. Transverse tensile (matrix tensile fracture) in the 45° to 90° load-angle range.
   d. Mixed mode (intralaminar shear and transverse tensile) in the 20° to 45° load-angle range.

6. Uniaxial strengths can be determined indirectly from sensitivity studies and the plotting procedure described herein. The intralaminar fracture shear stress was determined to be 5.5×10^{3} N/cm^{2} (8 ksi). This value is in good agreement with literature values 5.2×10^{3} to 6.2×10^{3} N/cm^{2} (7 5 to 9 0 ksi).

7. Linear composite mechanics can be used with confidence to describe quantatively the mechanical response to off-axis tensile loads of high-modulus-fiber/epoxy-matrix composites which exhibit linear stress-strain behavior to fracture.

8. The fracture modes and fracture surface characteristics in off-axis tensile specimens can be identified and quantified by using a combination of scanning electron microscopy, linear composite mechanics, and the plotting procedures described herein. Furthermore, this combination should be helpful for establishing comparable procedures for angle-plied laminates.

9. Criteria that can be used to identify fracture modes from fracture surface characteristics of off-axis fiber/resin composites are as follows:

a. Tiered surface with dominant fiber fractures is characteristic of longitudinal tensile fracture.
b. Smooth surface with matrix lacerations indicates intralaminar shear fracture.
c. Smooth surface with matrix cleavage indicates transverse tensile fracture.

REFERENCES

1. J. H. Sinclair, and C. C. Chamis, "Mechanical Behavior and Fracture Characteristics of Off-Axis Fiber Composites. I - Experimental Investigation," NASA TP-1081, 1977.

2. C. C. Chamis, and J. H. Sinclair, "Mechanical Behavior and Fracture Characteristics of Off-Axis Fiber Composites. II - Theory and Comparisons," NASA TP-1082, 1978.

3. J. H. Sinclair, and C. C. Chamis, "Fracture Surface Characteristics of Off-Axis Composites," Recent Advances in Engineering Science, G. C. Sih, ed., Proceedings of the 14th Annual Meeting of the Society of Engineering Science, Lehigh University, 1977, pp. 247-249. (Also NASA TM-73700, 1977.)

4. C. C. Chamis, and J. H. Sinclair, "The Effects of Eccentricities on the Fracture of Off-Axis Composites," Proceedings of the 33rd Annual Conference of the Society of the Plastics Industry Reinforced Plastics/ Composites Institute, Society of the Plastics Industry, Inc., 1978, Section 22A, pp. 1-6. (Also NASA TM-73826, 1978.)

5. C. C. Chamis, "Computer Code for the Analysis of Multilayered Fiber Composites - Users Manual," NASA TN D-7013, 1971.

6. C. C. Chamis, "Failure Criteria for Filamentary Composites," NASA TN D-5367, 1969.

7. C. C. Chamis, and J. H. Sinclair, "10^{o} Off-Axis Tensile Test for Intralaminar Shear Characterization of Fiber Composites," NASA TN D-8215, 1976.

8. G. J. Schneider, "Evaluation of Laminar Strength Criteria by Off-Axis Tensile Coupon Tests," Fibre Science Technol., vol. 5, no. 1, Jan. 1972, pp. 29-35.

TABLE I. - SUMMARY OF MEASURED DATA MODMOR I/EPOXY CENTER GAGE

Specimen	Load angle, deg	Specimen[a] thickness		Fracture load		Fracture stress		Fracture strain, ε_{xx}, percent	Modulus		Poisson's ratio	Coupling coefficient
		cm	in.	N	lb	N/cm^2	ksi		N/cm^2	psi		
A-0	0	0.135	0.053	9572	2152	56.3×10^3	81.7	0.231	24.1×10^6	34.9×10^6	0.27	0
A-5	5	.142	.056	6850	1540	38.0	55.2	.188	20.2	29.3	.22	2.8
A-10	10	.142	.056	6183	1390	34.3	49.8	.286	12.3	17.8	.16	3.3
A-15	15	.142	.056	3550	798	19.8	28.7	.284	7.18	10.4	.20	2.6
A-30	30	.145	.057	1588	357	8.8	12.7	.365	2.41	3.49	.19	1.4
A-45	45	.142	.056	934	210	5.0	7.5	.390	1.36	1.97	.19	.82
A-60	60	.142	.056	712	160	3.9	5.7	.413	.305	1.31	.09	.38
A-75	75	.145	.057	569	128	3.1	4.5	.385	.829	1.20	.05	.21
A-90	90	.132	.052	463	104	2.8	4.0	.364	.772	1.12	.01	0

[a]Nominal specimen width, 1.27 cm (0.500 in.).

TABLE II. - COMPARISON OF PREDICTED AND MEASURED FRACTURE STRAINS FOR MOD I/E UNIDIRECTIONAL COMPOSITE TESTED AT VARIOUS ANGLES TO THE FIBER DIRECTION

0.50 Fiber volume fraction

Specimen	Load angle, deg	Fracture strains, percent					
		Measured[a]			Predicted		
		Axial, ε_{cxx}	Poisson's, ε_{cyy}	Shear, ε_{cxy}	Axial, ε_{cxx}	Poisson's, ε_{cyy}	Shear, ε_{cxy}
A-0	0	0.231	-0.063	0.0025	0.269	-0.070	0
A-5	5	.188	-.047	.523	.234	-.062	.599
A-10	10	.287	-.046	.985	.351	-.093	1.05
A-15	15	.284	-.057	.743	.331	-.086	.868
A-30	30	.365	-.072	.522	.413	-.093	.596
A-45	45	.390	-.074	.319	.431	-.071	.341
A-60	60	.414	-.030	.152	.445	-.042	.182
A-75	75	.385	-.018	.081	.407	-.014	.069
A-90	90	.364	-.005	.004	.377	-.003	0

[a] ε_c from center gage.

TABLE I. - UNIDIRECTIONAL COMPOSITE PROPERTIES

Property	Manufacturer's data	Lewis Research Center data[a]
Longitudinal tensile:		
Strength, $S_{\ell 11T}$, N/cm^2 (ksi)	53.75×10^3 (78.0)	56.3×10^3 (81.7)
Modulus, $E_{\ell 11T}$, N/cm^2 (psi)	22.5×10^6 (32.6×10^6)	24.1×10^6 (34.9×10^6)
Poisson's ratio, $\nu_{\ell 12}$	0.184	0.27
Transverse tensile:		
Strength, $S_{\ell 22T}$, N/cm^2 (ksi)	4.07×10^3 (5.82)	2.8×10^3 (4.0)
Modulus, $E_{\ell 22T}$, N/cm^2 (psi)	0.70×10^6 (1.10×10^6)	0.772×10^6 (1.12×10^6)
Poisson's ratio, $\nu_{\ell 21}$	0.0039	0.01
Longitudinal compression:		
Strength, $S_{\ell 11C}$, N/cm^2 (ksi)	45.6×10^3 (66.2)	----------
Modulus, $E_{\ell 11C}$, N/cm^2 (psi)	35.8×10^6 (52×10^6)	----------
Poisson's ratio	0.31	----------
Transverse compression:		
Strength, $S_{\ell 22C}$, N/cm^2 (ksi)	20×10^3 (29)	----------
Modulus, $E_{\ell 22C}$, N/cm^2 (psi)	1.25×10^6 (1.82×10^6)	----------
Poisson'ratio	0.0083	----------
Shear:		
Strength, $S_{\ell 12S}$, N/cm^2 (ksi)	4.49×10^3 (6.52)	5.51×10^3 (8.0)
Modulus, $G_{\ell 12}$, N/cm^2 (psi)	0.489×10^6 (0.709×10^6)	0.610×10^6 (0.89×10^6)

[a]Center gage.

E-1235

TABLE II. - PREDICTED PLY FRACTURE STRAINS

FOR MOD I/E UNIDIRECTIONAL COMPOSITE

AS A FUNCTION OF LOAD ANGLE

Specimen	Load angle, deg	Composite fracture strain,[a] percent	Ply strains, percent		
			$\varepsilon_{\ell 11}$	$\varepsilon_{\ell 22}$	$\varepsilon_{\ell 12}$
A-0	0	0.231	0.269	-0.0698	0
A-5	5	.188	.180	- .007	.642
A-10	10	.287	.158	.100	1.14
A-15	15	.284	.0864	.159	.961
A-30	30	.365	.0286	.291	.736
A-45	45	.390	.00913	.351	.502
A-60	60	.414	.00102	.402	.330
A-75	75	.385	- .0026	.396	.151
A-90	90	.364	- .0034	.377	0

[a]ε_{cxx}, center gage, experimental results.

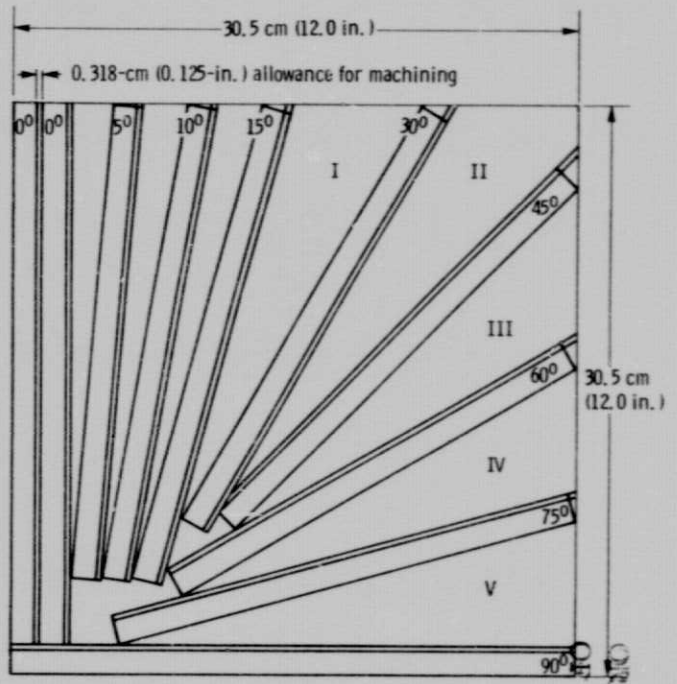

Figure 1. - Specimen layout on Mod I/E composite laminate plate.

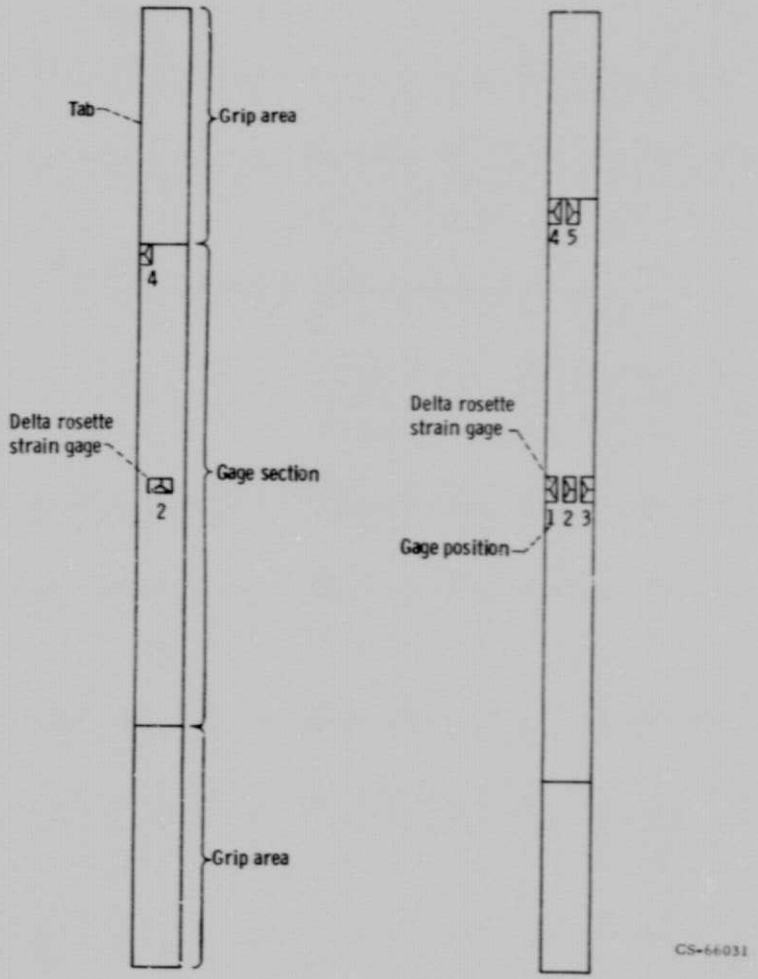

(a) Two-gage specimen.

(b) Five-gage specimen.

Figure 2. - Schematic of specimen geometry and strain-gage arrangement.

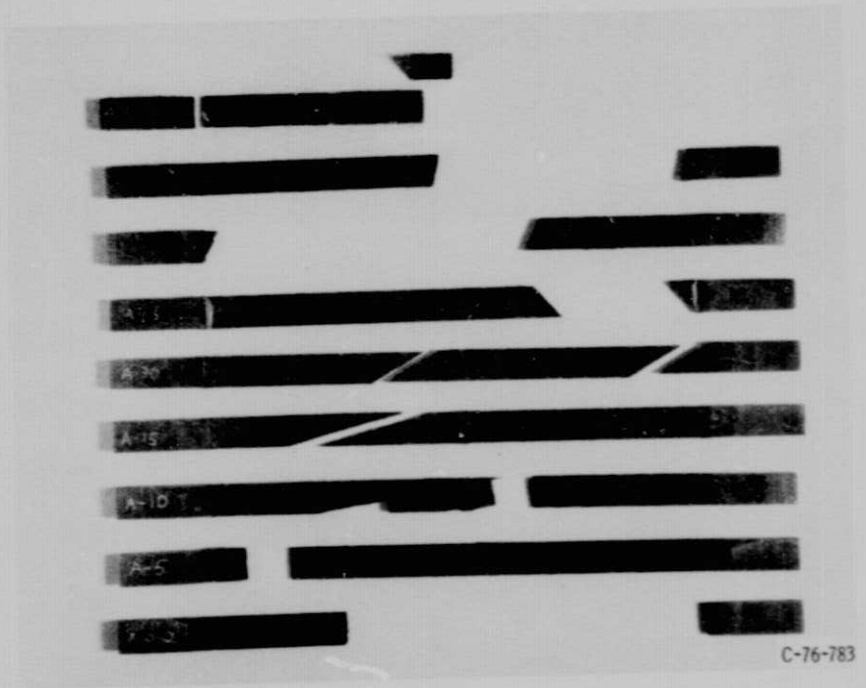

Figure 3. - Fractured tensile specimens.

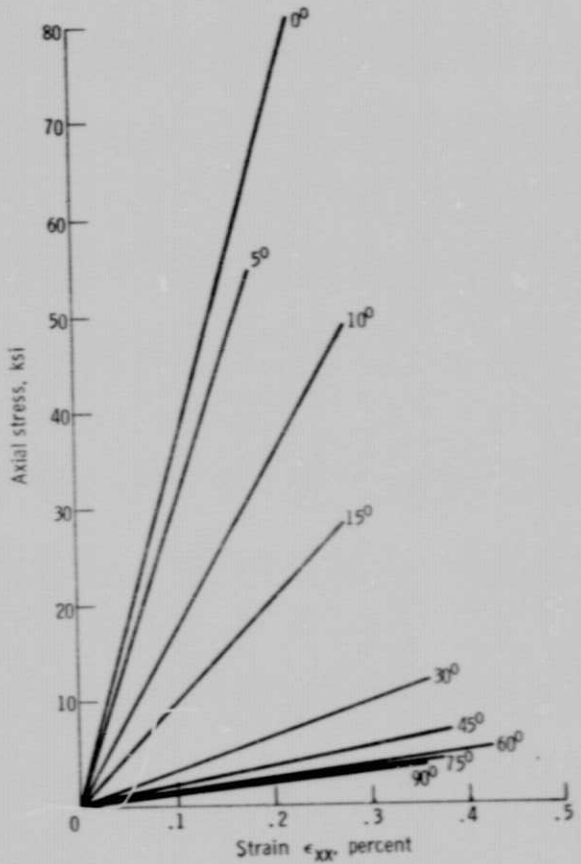

Figure 4. - Stress-strain curves for specimens subjected to tensile loading at various angles. (MOD I/E.)

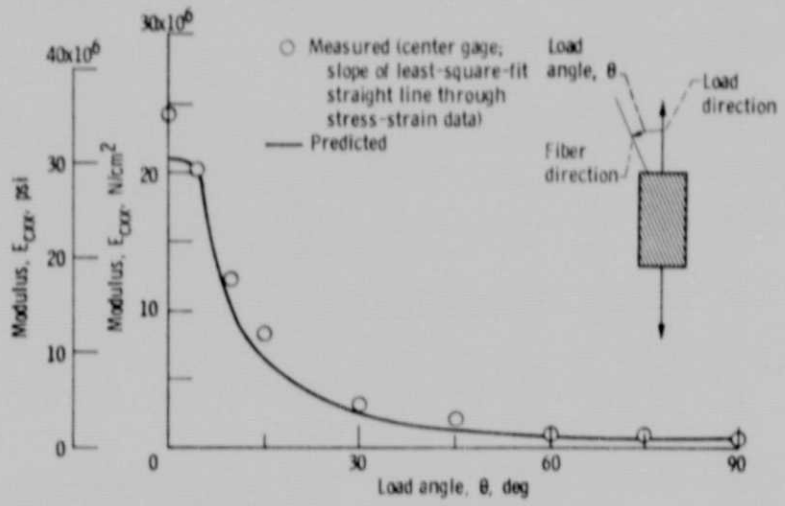

Figure 5. - Modulus for Mod I/E unidirectional composite tested at various angles to fiber direction.

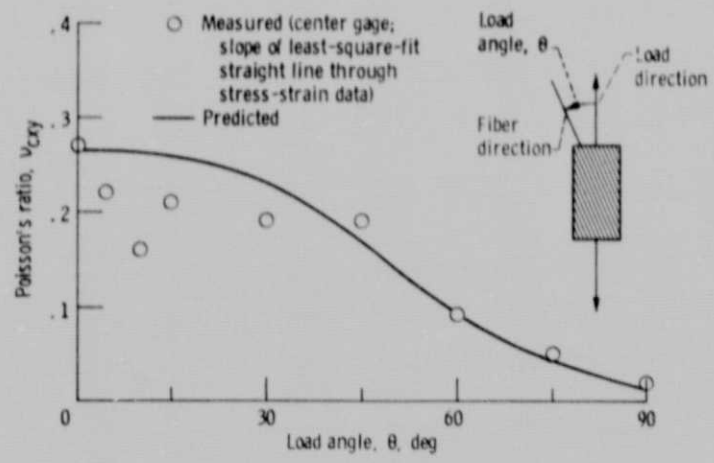

Figure 6. - Poisson's ratio for Mod I/E unidirectional composite tested at various angles to fiber direction.

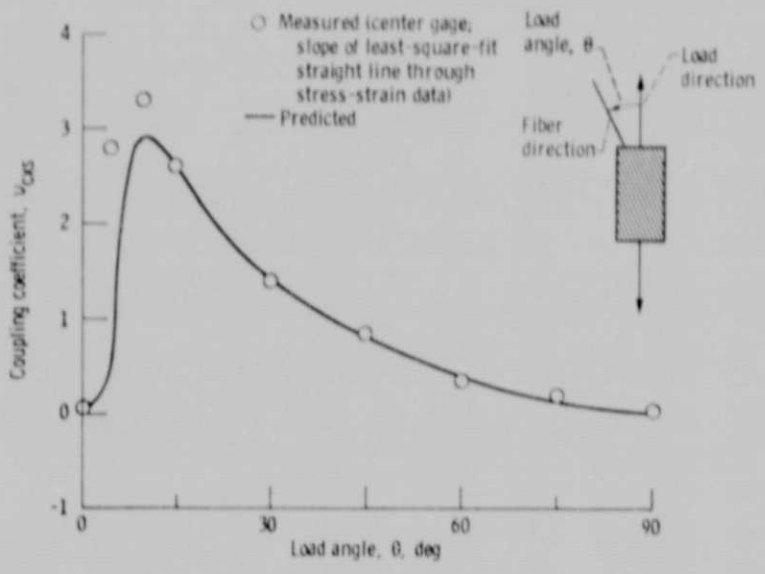

Figure 7. - Coupling coefficient for Mod I/E unidirectional composite tested at various angles to fiber direction.

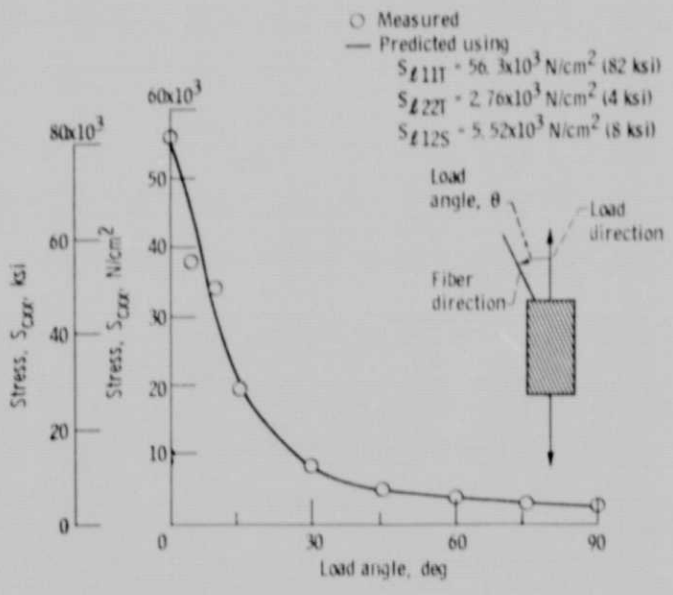

Figure 8. - Comparison of predicted and measured fracture stresses at various test angles for Mod I/E unidirectional composite.

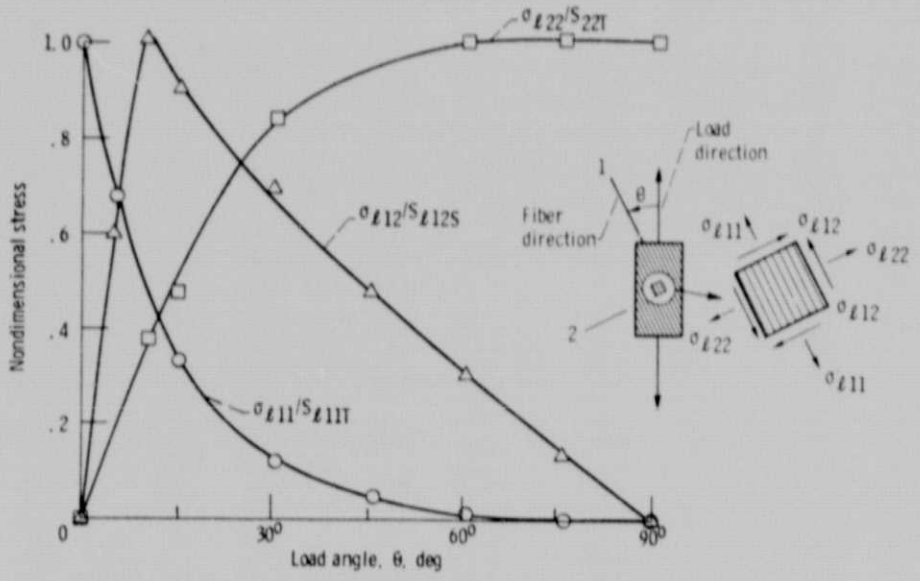

Figure 9. - Fracture stresses normalized with their respective uniaxial strengths (S_ℓ). (MOD I/E.)

(a) TEST ANGLE 0°, FIBER TENSION.

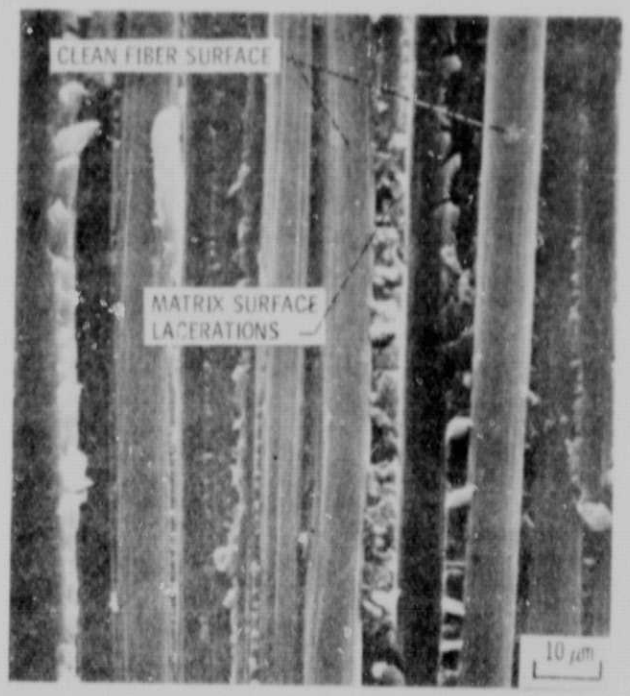

(b) TEST ANGLE 10°, INTRALAMINAR SHEAR.

(c) TEST ANGLE 90°, TRANSVERSE SECTION.

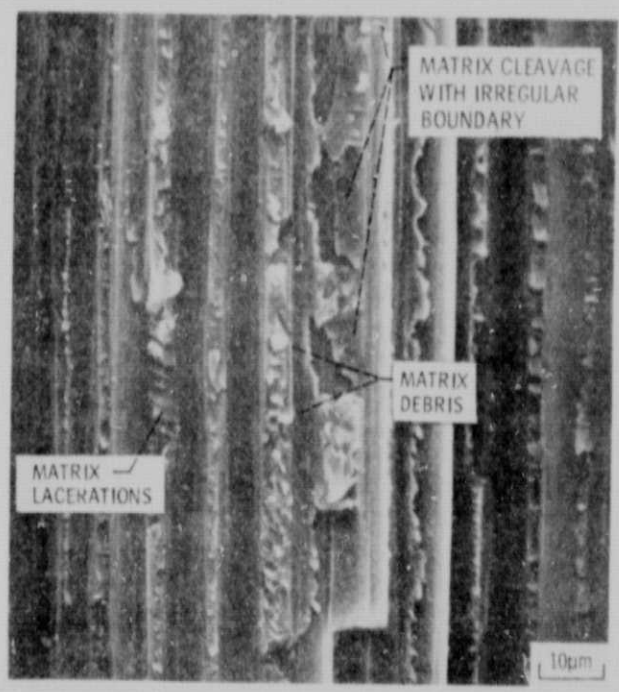

(d) TEST ANGLE 45°, MIXED INTRALAMINAR SHEAR AND TRANSVERSE TENSION.

Figure 10. - Fracture modes of Mod I/E found at various test angles (ref. 3).

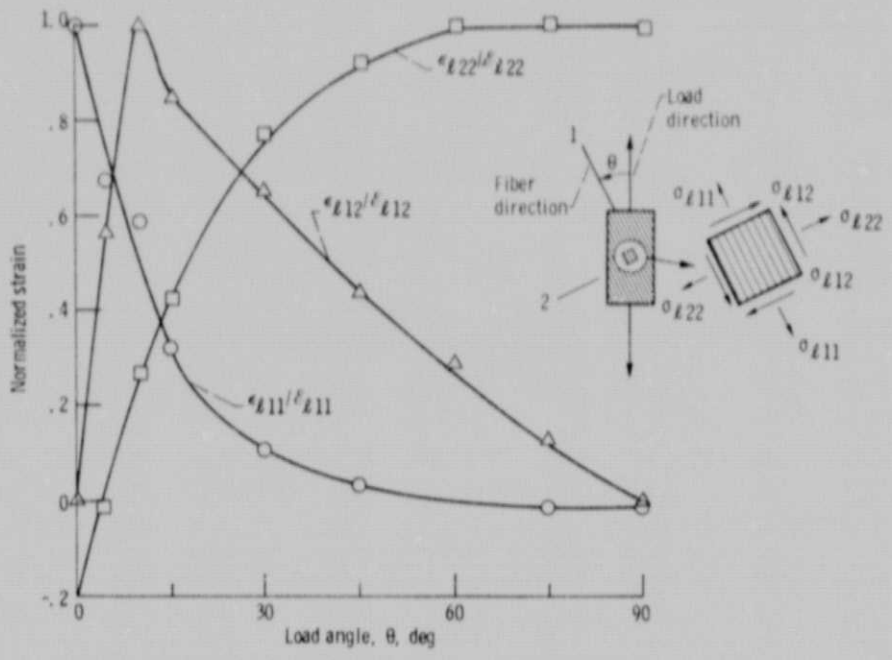

Figure 11. -Ply fracture strains normalized with their respective uniaxial fracture strains (Mod I/E).

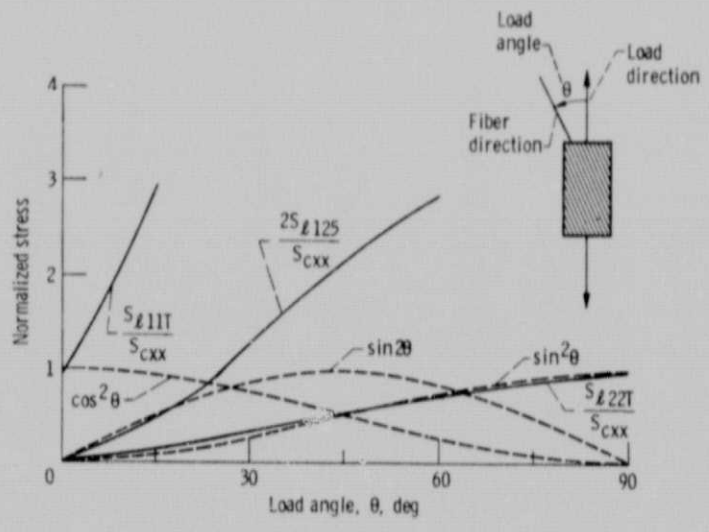

Figure 12. -Ply fracture stresses normalized with respect to specimen fracture stresses at various test angles (Mod I/E).

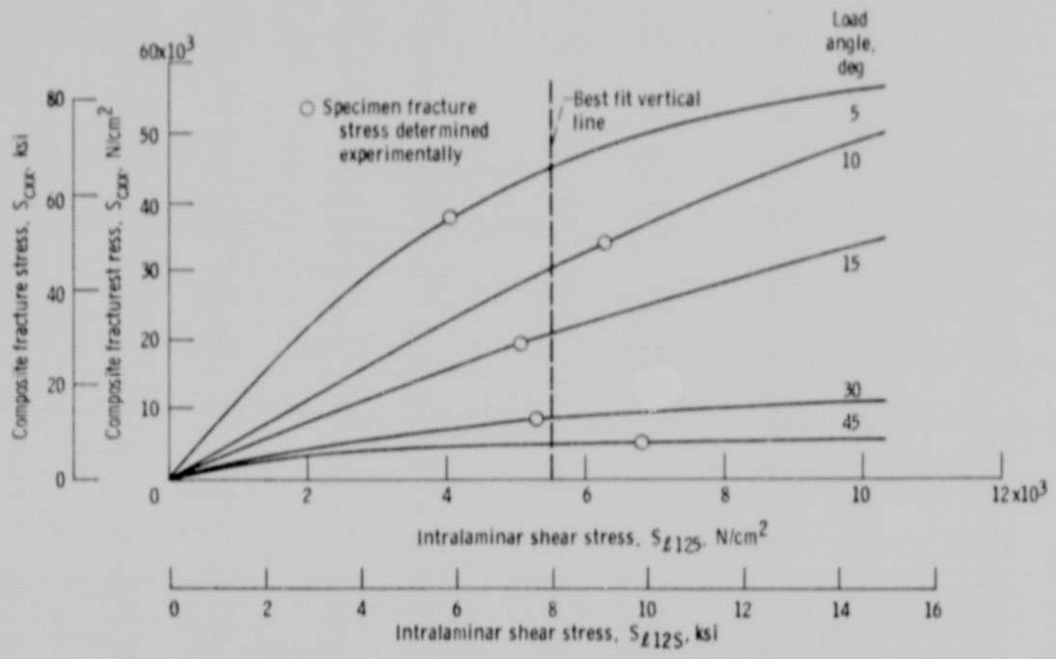

Figure 13. -Calculated fracture stresses for various assumed intralaminar shear stresses for Mod I/E unidirectional composite.